Crack tip transformation zones in austenitic stainless steel

Hallberg, Håkan; Banks-Sills, Leslie; Ristinmaa, Matti

Published in:
Engineering Fracture Mechanics

DOI:
10.1016/j.engfracmech.2011.11.004

2012

Engineering Fracture Mechanics 2012, 79(266-280)

Crack tip transformation zones in austenitic stainless steel

Håkan Hallberg*[1], Matti Ristinmaa[1], Leslie Banks-Sills[1,2]

[1] Division of Solid Mechanics, Lund University, Box 118, S-221 00 Lund, Sweden

[2] The Dreszer Fracture Mechanics Laboratory, School of Mechanical Engineering, The Fleischman Faculty of Engineering, Tel Aviv University, 69978 Ramat Aviv, Israel

*hakan.hallberg@solid.lth.se

Abstract

Crack tip conditions in SUS 304 austenitic stainless steel are studied using a constitutive model in which the martensitic phase transformation is an integral part. The phase transformation occurring in the crack tip region gives rise to fracture toughening of the material whereby the resistance against crack initiation, as well as the macroscopic material response are strongly altered by the presence of a martensitic phase. The constitutive model employed herein permits studying the transformation zones under different isothermal conditions. Local crack tip conditions and related plastic deformation is confirmed to depend strongly on the varying extent of the martensitic phase transformation at different temperatures. The shape and size of the plastic and transformation zones in the neighborhood of the crack tip are obtained from numerical simulations, as well as derived analytically.

Keywords: Steels, Constitutive modeling, Phase transformation, 304 stainless steel, Transformation toughening

Nomenclature

The nomenclature and mathematical operators used in the present paper are summarized in Table 1.

1 Introduction

Austenitic stainless steels are of major engineering importance in many applications due to their excellent mechanical properties over a wide range of temperatures in combination with good corrosion resistance. This class of steels is also susceptible to diffusionless phase

DOI: 10.1016/j.engfracmech.2011.11.004

Table 1: Nomenclature.

Parameter	Description
b	Parameter controlling the non-roundness of the transformation potential surface
$\boldsymbol{b}^{\mathrm{r}}$	Reversible part of the left Cauchy-Green tensor
c_i	Parameters in the transformation threshold function
$c_{\mathrm{p}}^{\mathrm{a,m}}$	Specific heat of the austenite and martensite phase, respectively
E	Elastic modulus
f	Yield function
F_{mech}	Mechanical transformation driving force
$\widetilde{F}_{\mathrm{mech}}$	θ-dependent components of F_{mech} from the HRR solution
$\breve{F}_{\mathrm{mech}}$	θ-dependent components of F_{mech} from the linear elastic solution
F_{chem}	Chemical transformation driving force
F_{trans}	Transformation threshold function
$\boldsymbol{F}$, $\boldsymbol{F}^{\mathrm{r}}$, $\boldsymbol{F}^{\mathrm{ir}}$	Deformation gradient, its reversible and irreversible components
G	Shear modulus
h	Transformation potential function
I_1	First invariant of the stress tensor
J_2, J_3	Second and third invariants of the deviatoric stress tensor
J^{r}	Determinant of the reversible deformation gradient
K	Bulk modulus
$\bar{K}$	Parameter in the transformation potential function
K_I	Mode I stress intensity factor
K_σ	Stress amplitude parameter in the HRR field
$\boldsymbol{l}$, $\boldsymbol{l}^{\mathrm{r}}$, $\boldsymbol{l}^{\mathrm{ir}}$, $\boldsymbol{l}^{\mathrm{p}}$, $\boldsymbol{l}^{\mathrm{tr}}$	Spatial velocity gradient, its reversible, irreversible, plastic and transformational components
n	Exponent in the Ramberg-Osgood hardening law
$r_{\mathrm{pl,tr}}$	Radius of the plastic and of the transformed zone, respectively, at the crack tip
r, θ	Polar crack tip coordinates
R, R_{ct}	Radius of the FE-analysis domain and of the inner crack tip region, respectively
s	Function of the Ramberg-Osgood exponent n
$s_0^{\mathrm{a,m}}$	Entropy of the austenite and martensite phase, respectively
T, T_0	Absolute temperature and absolute reference temperature
u_x, u_y	Displacement components in the x- and y-directions, respectively
x, y	Cartesian crack tip coordinates
$\hat{x}$, $\hat{y}$	Normalized Cartesian crack tip coordinates
z	Volume fraction of martensite
α	Coefficient in the Ramberg-Osgood hardening law
δ	Parameter controlling the pressure dependence of the transformation surface
$\varepsilon_{\mathrm{eff}}^{\mathrm{p}}$	Effective plastic strain
ϕ	Angular crack tip function
ρ_0	Mass density
σ_{eff}	Effective stress
σ_{ij}, $\hat{\sigma}_{ij}$	Stress tensor components and the normalized counterpart
$\widetilde{\sigma}_{ij}$	Angular dependence of the crack tip stress components from the HRR solution
$\breve{\sigma}_{ij}$	Angular dependence of the crack tip stress components from the linear elastic solution
$\boldsymbol{\tau}$	Kirchhoff stress tensor
ν	Poisson's ratio
$(\cdot) : (\cdot)$	Tensorial contraction over two indices
$\mathrm{tr}(\cdot)$	Tensorial trace
$\mathrm{sym}(\cdot)$	The symmetric part of a tensor
$(\cdot)^{\mathrm{dev}}$	The deviatoric part of a tensor
$\dot{(\cdot)}$	Material derivative with respect to time
$(\cdot)_{\mathrm{i}}$	Isochoric part of a tensor
$(\cdot)^{-1}$	Inverse of a tensor

transformation of the austenitic face-centered cubic parent phase into body-centered cubic or body-centered tetragonal martensite under applied deformation. This very rapid transformation is promoted by a lowering of the temperature while higher temperatures restrict martensite formation [1]. Since austenitic stainless steels are used for example in power generating and chemical industries, low-temperature service conditions for these materials are indeed common. If the loading situation is such that fracture is initiated in the material, formation of martensite at the crack tip may delay or even prevent further crack propagation. The increase in fracture toughness due to martensite formation, which has been frequently observed e.g. in [1, 2, 3, 4, 5, 6, 7, 8], is somewhat surprising since the hard martensitic phase is considerably more brittle than the ductile austenite. This transformation toughening and reduction of crack growth rate has been attributed to crack tip shielding and crack tip blunting [9], and crack closure due to roughening of the crack surfaces or due to the crack being subjected to compression by the dilatation in the transformed material [10, 11]. In addition, several authors point out that the strongly dissipative process of martensitic phase transformation reduces the energy available at the crack tip for extending the crack [2]. On a micromechanical level, crack initiation is delayed since void nucleation is reduced by the phase transformation, cf. [12], and the growing martensitic phase restricts subsequent void growth [13].

It is also noted that the fracture toughness is not a strictly increasing function of the volume fraction of transformed material, but also a function of temperature, strain rate and the absolute size of the martensite islands that are formed [14, 15]. Regarding the latter, based on experimental observations, it was proposed in [16] that smaller regions of martensite restrict the load transfer to the martensite while larger martensite islands carry more load, and hence are more likely to fracture. Similar observations are made in [17]. In [15], it is noted that substantial enhancement of the fracture toughness seems to occur for intermediate volume fractions of martensite, 30-60%, above which the enhancing effect levels off. At higher volume fractions of martensite, the ductility of the material is found to be severely degraded by the extensive presence of hard martensite [17]. Transformation of austenite into martensite has also been observed in relation to hydrogen embrittlement of dual-phase steel by sensitizing the austenite grain boundaries to hydrogen. Subsequent fracture then progresses along these boundaries [1]. Regarding the appearance of the transformation zones in the vicinity of a crack-tip, it is observed in [2] that the shape of the transformation zones resembles the butterfly shape of the plastic zone. In addition, it is noted in [1] that the transformation zones are smaller than the plastic zone. This is, however, dependent on the temperature since only small amounts of martensite are formed at higher temperatures despite extensive plastic deformation of the austenite [1].

Simulations of fracture influenced by martensitic phase transformation in relation to shape memory alloys has been studied in [18, 19, 20] and modeling of phase transformation in relation to fracture in austenitic stainless steel may be found in [21, 22]. However, to

the authors' knowledge, detailed studies of the transformation zones and their influence on the crack tip properties in stainless steel does not exist. Hence, analyses of this kind are the focus of the present paper. The presented work exploits a constitutive model that was previously developed in [23, 24]. The model describes finite strain elasto-plasticity taking the martensitic phase transformation into account. Parameters are calibrated using material data on SUS 304 austenitic stainless steel. This allows crack tip conditions under the influence of phase transformation in this material to be studied through finite element (FE) analyses of a disc-shaped body. In addition, the appearance of the transformation zones in the vicinity of the crack tip is obtained analytically. For comparison also the plastic zones are obtained analytically, as well as through FEs. Noting that the transformed region is small in comparison with the plastic zone at room temperature and above, crack tip conditions are governed by the J-integral rather than the K_I stress intensity factor under these circumstances. In the present work, the Hutchinson-Rice-Rosengren (HRR) solution to the J-dominated crack tip stress field is used as an alternative approach to analytically determine the size and shape of the transformation zones [25, 26].

This paper is organized as follows. In Section 2, the constitutive model is briefly summarized. In Section 3, finite element simulations of the crack tip zones under plane strain mode I conditions and at different temperatures are studied, both with and without phase transformation. Martensite and austenite transformation zones together with the plastic zones are determined analytically using the elastic K_I field in Section 4 and using the Hutchinson-Rice-Rosengren plasticity solution in Section 5. Some concluding remarks in Section 6 close the paper.

2 Constitutive model

The constitutive model employed in the present study was previously established in the preceding papers [23, 24] and is for completeness outlined in this section. The constitutive model is a phenomenological, continuum mechanical formulation, based on a multiplicative split of the deformation gradient $\boldsymbol{F}$ into one component related to the reversible processes of elastic and thermal deformation – denoted by a superscript r – and one component related to the irreversible processes of plastic slip and phase transformation – denoted by a superscript ir, i.e. $\boldsymbol{F} = \boldsymbol{F}^{\mathrm{r}}\boldsymbol{F}^{\mathrm{ir}}$. The elastic behavior of the model is given by a Neo-Hookean type strain energy density function

$$W = \frac{1}{2}K\left[\frac{1}{2}\left\{\left(J^{\mathrm{r}}\right)^2 - 1\right\} - \ln\left(J^{\mathrm{r}}\right)\right] + \frac{1}{2}G\left[\mathrm{tr}\left(\boldsymbol{b}_{\mathrm{i}}^{\mathrm{r}}\right) - 3\right] \tag{1}$$

where $J^{\mathrm{r}} = \det\left(\boldsymbol{F}^{\mathrm{r}}\right)$ is the determinant of the reversible deformation gradient, G and K are the shear and bulk moduli, respectively. Here $\boldsymbol{b}_{\mathrm{i}}^{\mathrm{r}} = \boldsymbol{F}_{\mathrm{i}}^{\mathrm{r}}\boldsymbol{F}_{\mathrm{i}}^{\mathrm{r}T}$ is chosen to denote the isochoric part of the reversible left Cauchy-Green tensor where $\boldsymbol{F}_{\mathrm{i}}^{\mathrm{r}} = \left(J^r\right)^{-\frac{1}{3}}\boldsymbol{F}^{\mathrm{r}}$. The trace

of a tensorial quantity is given by tr $(\cdot)$. From the strain energy density function in eq. (1), the Kirchhoff stress tensor can be obtained as

$$\boldsymbol{\tau} = G\boldsymbol{b}_{\mathrm{i}}^{\mathrm{r,dev}} + \frac{1}{2}K\left(J^{\mathrm{r}2} - 1\right)\mathbf{1} \tag{2}$$

where $\mathbf{1}$ is the second-order identity tensor and where $(\cdot)^{\mathrm{dev}}$ indicates the deviatoric part of a tensor.

Turning next to the irreversible behavior of the model, the spatial velocity gradient is denoted by $\boldsymbol{l} = \dot{\boldsymbol{F}}\boldsymbol{F}^{-1}$ where a superposed dot indicates the material derivative with respect to time. Using the previous multiplicative split of the deformation gradient, the spatial velocity gradient may be written using its reversible and irreversible parts as $\boldsymbol{l} = \boldsymbol{l}^{\mathrm{r}} + \boldsymbol{l}^{\mathrm{ir}}$ where the irreversible, spatial, part is given by $\boldsymbol{l}^{\mathrm{ir}} = \boldsymbol{F}^{\mathrm{r}}\dot{\boldsymbol{F}}^{\mathrm{ir}}(\boldsymbol{F}^{\mathrm{ir}})^{-1}(\boldsymbol{F}^{\mathrm{r}})^{-1} = \boldsymbol{l}^{\mathrm{p}} + \boldsymbol{l}^{\mathrm{tr}}$. The component related to plastic slip is denoted by a superscript p and the component related to phase transformation is denoted by a superscript tr. This decomposition allows deformation due to plastic slip and deformation due to phase transformation to occur independently of each other. If active at the same time, however, plasticity and phase transformation will influence each other. Adopting incremental J_2-plasticity the effective stress is defined as $\sigma_{\mathrm{eff}} = (3J_2)^{1/2}$ and the yield function is found as

$$f = \sigma_{\mathrm{eff}} - \sigma_{\mathrm{y}}\left(T, \varepsilon_{\mathrm{eff}}^{\mathrm{p}}, z\right) \leq 0 \tag{3}$$

where $\sigma_{\mathrm{y}}\left(T, \varepsilon_{\mathrm{eff}}^{\mathrm{p}}, z\right)$ is related to the hardening behavior of the material with an initial value $\sigma_{\mathrm{y0}}\left(T\right) = \sigma_{\mathrm{y}}\left(T, 0, 0\right)$. Although the temperature is present in eq. (3), only isothermal conditions are considered in the present work and the temperature T is taken as a constant parameter. The plastic zone is defined by $f = 0$. The temperature dependence of σ_{y0} is taken according to [24], giving

$$\sigma_{\mathrm{y0}}\left(T\right) = 609 - 1.25T \quad \mathrm{MPa} \tag{4}$$

Since this expression is obtained at $z = 0$, it corresponds to the initial yield stress of the austenitic phase. Letting sym $(\cdot)$ denote the symmetrical part of a tensor, the evolution of the plastic slip deformation is found as

$$\mathrm{sym}\left(\boldsymbol{l}^{\mathrm{p}}\right) = \frac{3}{2}\frac{\boldsymbol{\tau}^{\mathrm{dev}}}{\sigma_{\mathrm{eff}}}\dot{\varepsilon}_{\mathrm{eff}}^{\mathrm{p}} \tag{5}$$

In eq. (5), $\dot{\varepsilon}_{\mathrm{eff}}^{\mathrm{p}} = \left[\frac{2}{3}\mathrm{sym}\left(\boldsymbol{l}^{\mathrm{p}}\right) : \mathrm{sym}\left(\boldsymbol{l}^{\mathrm{p}}\right)\right]^{\frac{1}{2}}$ is the effective plastic strain rate. The notation $(\cdot) : (\cdot)$ denotes a tensorial contraction over two indices. The second invariant of the deviatoric stress tensor is defined by $J_2 = \frac{1}{2}\mathrm{tr}\left(\boldsymbol{\tau}^{\mathrm{dev}}\boldsymbol{\tau}^{\mathrm{dev}}\right)$. The phase transformation in the model is assumed to be governed by a transformation function

$$h = F_{\mathrm{mech}} + F_{\mathrm{chem}} - F_{\mathrm{trans}} \leq 0 \tag{6}$$

where F_{mech} and F_{chem} are the mechanical and chemical driving forces and where F_{trans} is a threshold value for phase transformation, much like the yield stress in standard plasticity models. The transformation zone is in this way defined by $h = 0$. The mechanical thermodynamic driving force for phase transformation is given by

$$F_{\text{mech}} = \bar{K}\left(\bar{\sigma}_{\text{eff}} + \frac{1}{3}\delta I_1\right) \quad \text{where} \quad \bar{\sigma}_{\text{eff}} = \left(3J_2 + 3b\frac{J_3}{J_2^{1/2}}\right)^{1/2} \tag{7}$$

In eq. (7), $\bar{K}$, δ and b are material parameters and the first invariant of the stress tensor is denoted by $I_1 = \text{tr}\,(\boldsymbol{\tau})$ while the third invariant of the deviatoric stress tensor is given by $J_3 = \frac{1}{3}\text{tr}\left(\boldsymbol{\tau}^{\text{dev}}\boldsymbol{\tau}^{\text{dev}}\boldsymbol{\tau}^{\text{dev}}\right)$. It can be noted that F_{mech} contains both volumetric and deviatoric components by the presence of the I_1-invariant and the J_2- and J_3-invariants, respectively. As is shown in detail in [23], the transformation surface h in eq. (6) is calibrated through a procedure where the 24 crystallographically possible variants of martensite and the associated transformation strains are considered. By this approach, the parameters δ and b can be calibrated to fit the behavior of a polycrystalline material undergoing a martensitic transformation from fcc to bct structure. The δ-parameter controls the dependence on deviatoric stresses, i.e. the transformation shear deformation, and the b-parameter controls the influence of hydrostatic pressure, i.e. b is related to the volumetric deformation component. If both δ and b are put to zero, a surface corresponding to the yield surface in J_2 plasticity is obtained.

The chemical thermodynamic driving force for phase transformation is obtained as the difference between the chemical energies of the austenite and martensite phases, giving

$$F_{\text{chem}} = -\rho_0\left\{\left(s_0^{\text{a}} - s_0^{\text{m}}\right)(T - T_0) + \left(c_{\text{p}}^{\text{m}} - c_{\text{p}}^{\text{a}}\right)\left[(T - T_0) - T\ln\frac{T}{T_0}\right]\right\} \tag{8}$$

where T_0 is a reference temperature, c_{p} the specific heat and s_0 the entropy. Here and throughout the text, superscripts a and m indicate components related to the austenite and martensite phases, respectively. The transformation threshold F_{trans} is given by

$$F_{\text{trans}} = \bar{K}\left\{c_1 + c_2(T)\left[1 - \exp(-c_3 z)\right]\left[1 - c_4\ln(1 - z)\right]\right\} \tag{9}$$

where c_i are model parameters and where $z \in [0, 1]$ is the volume fraction of martensite in the material. In a purely austenitic material $z = 0$ and if only martensite is present $z = 1$. The evolution of the deformation related to phase transformation is obtained from the potential function in eq. (6) and appears as

$$\text{sym}\left(\boldsymbol{l}^{\text{tr}}\right) = \dot{z}\frac{\partial h}{\partial \boldsymbol{\tau}} \tag{10}$$

All components of the constitutive model are thereby defined. For a complete derivation of the above expressions, calibration of the parameters and for the numerical implementation,

refer to [23, 24]. For convenience, the calibrated material parameters are summarized in Table 2. The behavior of the model, compared to experimental data taken from [27], is shown in Fig. 1.

Following the definitions of "stress-assisted" and "strain-induced" martensitic phase transformation, as formulated in [28], the present model incorporates both of these processes since phase transformation and plasticity may occur independently of each other in the model, each being defined in stress-space by a transformation surface and a yield surface, respectively. This allows the two processes to be phenomenologically captured. It is noted that at stresses below the yield stress of austenite, phase transformation can take place in the model and result in "stress-assisted" phase transformation. Correspondingly, at stresses above the yield limit of austenite, phase transformation takes place together with plastic straining, giving "strain-induced" phase transformation. In addition, the parameter c_2 that varies with temperature, cf. Table 2, renders a formulation that allows phase transformation at low temperatures without plastic deformation while, at higher temperatures, increasing stress is required to drive phase transformation and hence increasing plastic deformation is present during the phase transformation. The $\bar{K}$-parameter is found when calibrating the transformation threshold function F_{trans} in eq. (9). This parameter is similar to the "Greenwood-Johnson" parameter as discussed in [29] and the calibration of this parameter is also shown in [23].

Table 2: Material parameters entering the present model. The values are valid for SUS 304 stainless steel and are taken from [23, 24].

Parameter	Value
G	77 GPa
K	167 GPa
ρ_0	7800 kg/m^3
$\bar{K}$	0.185
δ	0.29
b	0.35
T_0	440 K
$s_0^{\text{a}} - s_0^{\text{m}}$	0.106 J/kgK
c_1	1246 MPa
$c_2(T)$	$198 + \left(\frac{T}{214}\right)^{13.3}$ MPa
c_3	29.5
c_4	2.7
c_{p}^{a}	450 J/kgK
c_{p}^{m}	415 J/kgK

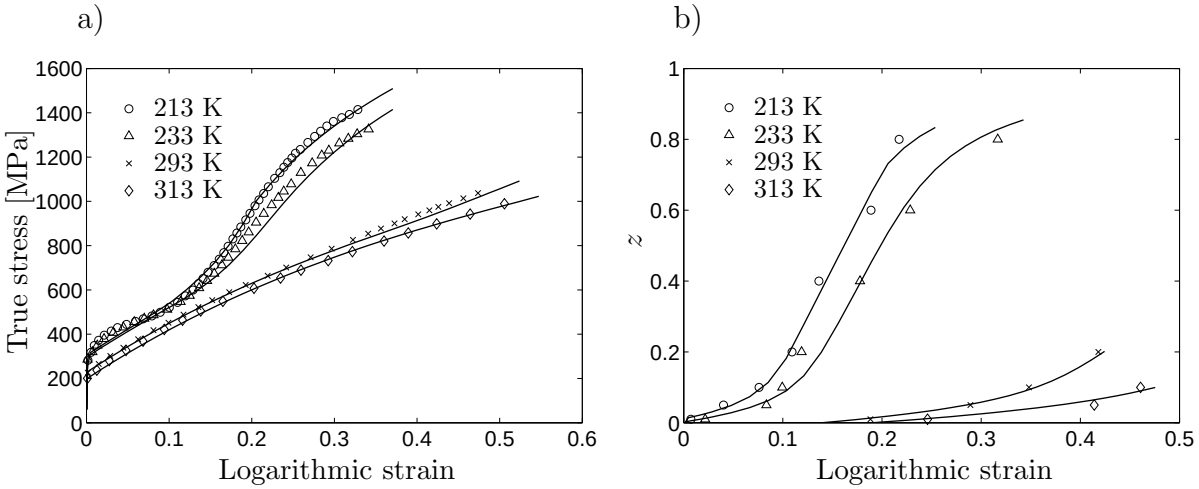

Figure 1: The response of the present constitutive model (solid lines) compared to experimental data (symbols) obtained from [27]: (a) shows the stress/strain response and (b) the corresponding volume fraction of martensite.

3 Plastic and transformed zones at the crack tip from FE simulations

The constitutive model is implemented as a user-defined subroutine in Abaqus Standard and material parameters are chosen according to [23, 24]. These parameters are summarized in Table 2. Assuming pure mode I deformation and plane strain conditions, a crack is modeled in a semi-circular geometry, taking advantage of symmetry. This is shown schematically in Fig. 2 together with the regions in which a coarse and a refined mesh are used, respectively. A total of 37,510 eight-noded, isoparametric, second order, elements of type CPE8 are used to discretize the full domain, whereof 16,800 in the coarse-meshed region and 20,710 in the fine-meshed region. Different mesh densities were investigated in order to verify that the shape and size of the obtained transformation zones were consistent. The planar linear elastic displacement field for a plane strain mode I crack is given by the in-plane displacement components

$$\begin{aligned} u_x &= \frac{K_I}{G}\sqrt{\frac{r}{2\pi}}\cos\left(\frac{\theta}{2}\right)\left[1-2\nu+\sin^2\left(\frac{\theta}{2}\right)\right] \\ u_y &= \frac{K_I}{G}\sqrt{\frac{r}{2\pi}}\sin\left(\frac{\theta}{2}\right)\left[2-2\nu-\cos^2\left(\frac{\theta}{2}\right)\right] \end{aligned} \tag{11}$$

where r and θ are the polar crack tip coordinates, as shown in Fig. 3. Also, the shear modulus G, the Poisson's ratio ν and the mode I stress intensity factor K_I were introduced in eq. (11). To facilitate comparison between different results, Cartesian crack tip coordinates

x and y are normalized according to

$$\hat{x} = \left(\frac{K_I}{\sigma_{y0}\left(T = 313\right)} \right)^{-2} x \qquad \text{and} \qquad \hat{y} = \left(\frac{K_I}{\sigma_{y0}\left(T = 313\right)} \right)^{-2} y \tag{12}$$

Note that the normalization factor contains the initial yield stress of the austenite phase at a temperature of $T = 313$ K, cf eq. (4). This normalization factor is kept constant for all isothermal conditions studied in the present work. The analysis region is chosen to be sufficiently large so that a small-scale yielding approximation is applicable. Boundary conditions are prescribed on the outer rim of the model in Fig. 2, by using the displacement components in eq. (11). In the present case, as shown in Fig. 2a, the semi-circular analysis domain is given an outer radius of $R = 200$ mm and $R_{\text{ct}} = 10$ mm is also used.

The plastic zones in the vicinity of the crack tip are shown in Fig. 4 at four different temperatures. Correspondingly, the transformation zones for $h\left(\boldsymbol{\sigma}, z = 0\right) = 0$, i.e. at the onset of phase transformation when $z = 0$, are shown in Fig. 5 for the two lower temperatures. The results in these figures are shown using normalized coordinates according to eqs. (12). Also, in both cases $K_I = 75$ MPa$\sqrt{\text{m}}$ and $K_I = 33$ MPa$\sqrt{\text{m}}$ are used. The former value is a characteristic value for the fracture toughness K_{Ic} for stainless steel at room temperature, cf. [14], and the latter value is chosen since FE calculations indicate that the plastic strains will then be at or below 10 %. The motivation for limiting the strains to this interval is further addressed in Section 5. The pointed appearance of the transformation zone in Fig. 5b is a result of the stress distribution around the crack tip which influences e.g. the I_1 and J_3 invariants of the transformation potential function given by eqs. (6) and (7). The strains due to plastic deformation and due to phase transformation are competing and this interaction manifests itself in the appearance of the zones in Figs. 4 and 5. This is especially evident for the temperature $T = 233$ K, cf. Figs. 4b and 5b, where the zones are of similar size. The interaction is, however, less obvious for the lower temperature of $T = 213$ K where the transformation zone is much larger than the plastic

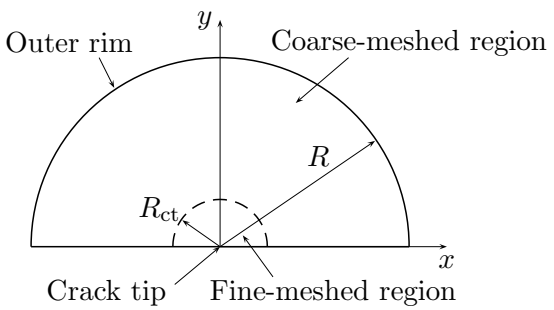

Figure 2: Geometry used for the FE model where $R = 200$ mm and $R_{\text{ct}} = 10$ mm (not drawn to scale).

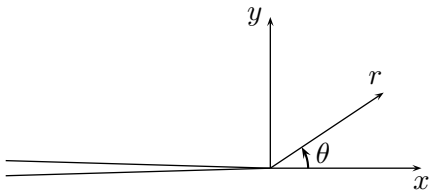

Figure 3: Definition of the polar crack tip coordinates r and θ.

zone and for the higher temperatures of $T = 293$ K and $T = 313$ K where the plastic zone completely dominates the transformation zone. The fully martensitic zones will be confined to very small regions close to the crack tip. Note that the transformation zones in Fig. 5 have a butterfly shape also observed experimentally in [2]. The expected trend is shown in Fig. 5 where the size of the transformed region is reduced as the temperature is increased. At the two higher temperatures of 293 K and 313 K, no phase transformation

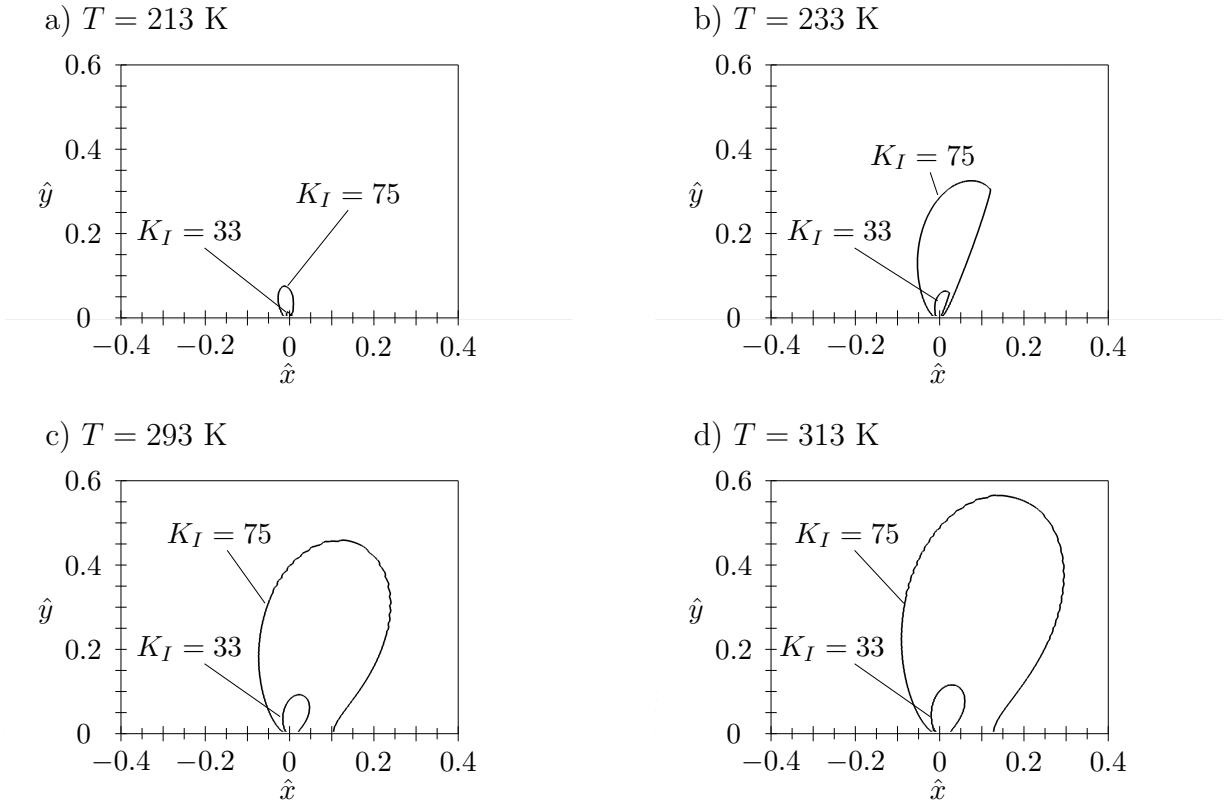

Figure 4: Plastic zone at the crack tip at four different temperatures. Results obtained from FE-simulations using $K_I = 33$ MPa$\sqrt{\text{m}}$ and $K_I = 75$ MPa$\sqrt{\text{m}}$, respectively. (a) $T = 213$ K, (b) $T = 233$ K, (c) $T = 293$ K and (d) $T = 313$ K.

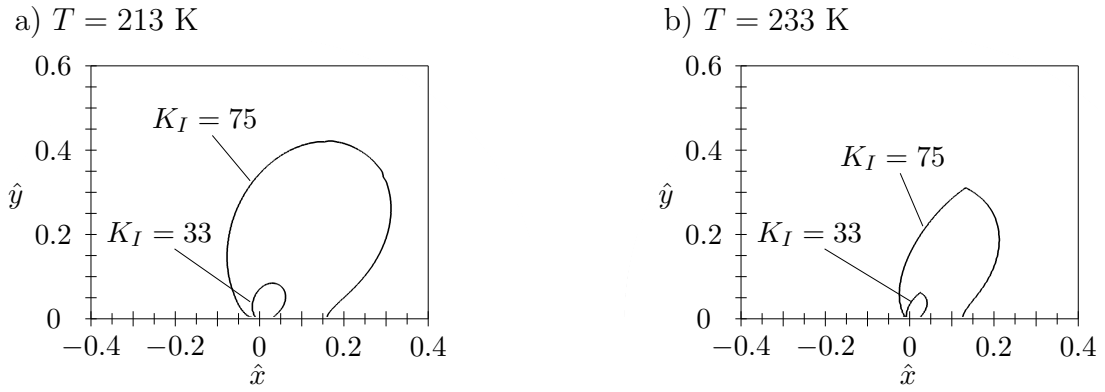

Figure 5: Transformed zone, corresponding to $z = 0$, at the crack tip at two temperatures. Results obtained from FE-simulations using $K_I = 33$ MPa$\sqrt{\text{m}}$ and $K_I = 75$ MPa$\sqrt{\text{m}}$, respectively. (a) $T = 213$ K, (b) $T = 233$ K. None or negligible phase transformation occurs at these load levels for the higher temperatures of 293 K and 313 K, also considered in the present work.

occurs at $K_I = 33$ MPa$\sqrt{\text{m}}$ and only negligibly at $K_I = 75$ MPa$\sqrt{\text{m}}$. The transformation zones at these temperatures are hence not shown. These observations are consistent with the experimental data shown in Fig. 1b where it is seen that additional strain is required to initialize phase transformation at these temperatures. It can also be noted from Figs. 4 and 5 that the shape of the zones are similar at both $K_I = 33$ MPa$\sqrt{\text{m}}$ and $K_I = 75$ MPa$\sqrt{\text{m}}$. This indicates that the lower value in fact can be used to obtain a fair representation of the zone shapes at higher load levels.

As found experimentally in [1] and also seen in Figs. 4 and 5, the transformation zones are large in comparison with the plastic zones at lower temperatures, whereas the opposite situation is found at higher temperatures. At these higher temperatures, the austenite may be exposed to extensive plastic deformation with only minor phase transformation taking place. In fact, at sufficiently high temperatures no phase transformation will take place at all, irrespective of the amount of plastic deformation imposed on the austenitic material. This is in contrast to the situation at low temperatures where phase transformation may occur simply due to a further lowering of the temperature, without any externally applied deformation of the austenite, i.e. without previous plastic deformation. This is characteristic of the metastable nature of the austenitic phase.

The variation of the crack opening stress σ_{yy} ahead of the crack tip at four different temperatures, both with and without phase transformation, is shown in Fig. 6. Note that at the lower temperatures the opening stress is reduced close to the crack tip in the presence of martensite (solid lines), compared to the purely austenitic material (dashed lines). This effect gradually vanishes as the temperature is increased, making the graphs coincide at the two higher temperatures of $T = 293$ K and $T = 313$ K in Figs. 6c and

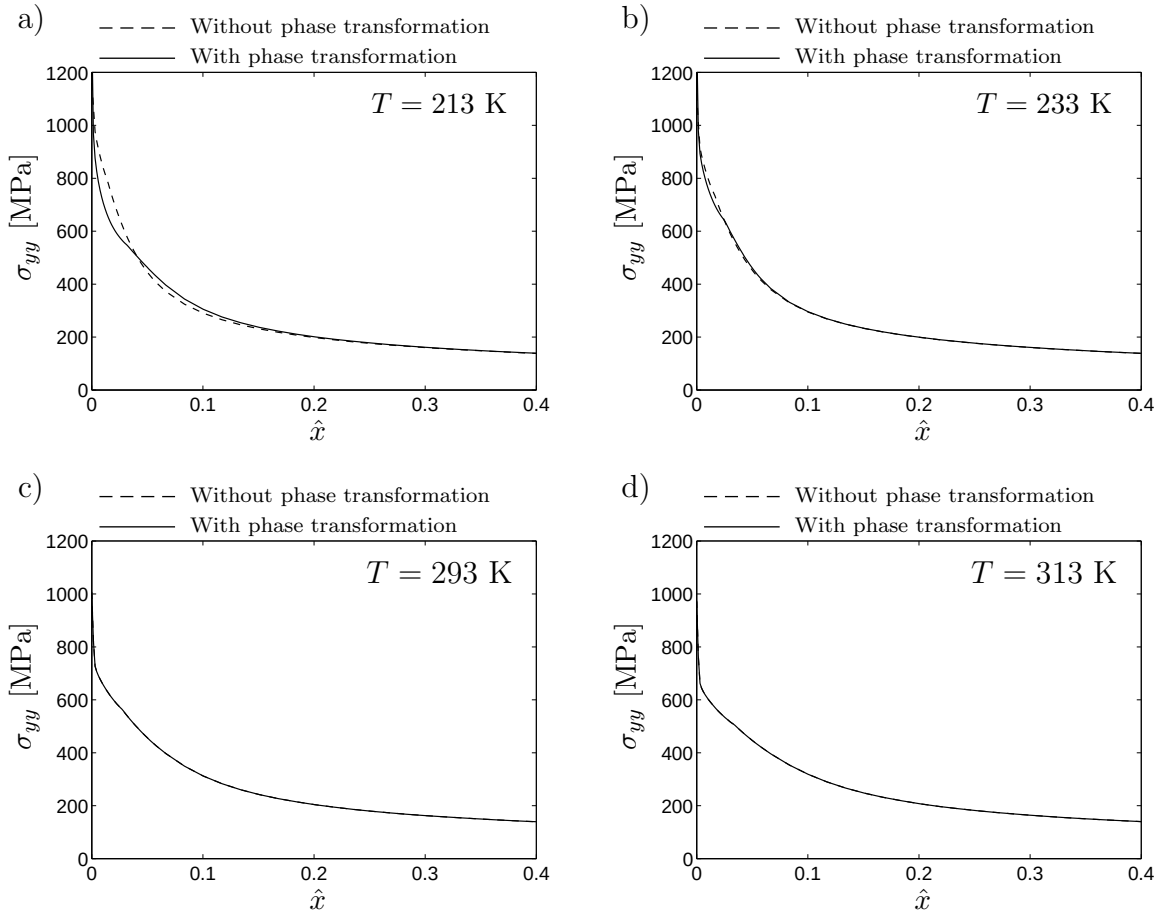

Figure 6: Mode I opening stress obtained from FE simulations at four different temperatures with $K_I = 75$ MPa$\sqrt{\text{m}}$. (a) $T = 213$ K, (b) $T = 233$ K, (c) $T = 293$ K and (d) $T = 313$ K. Solid lines show result with phase transformation and dashed lines show results without phase transformation.

6d. The stress variations shown in Fig. 6 illustrate the stress relief close to the crack tip caused by the martensitic phase transformation. The reduced opening stress ahead of the crack tip caused by phase transformation is one aspect of transformation toughening. The results in Fig. 6 are taken from FE simulations with $K_I = 75$ MPa$\sqrt{\text{m}}$ which, as was noted previously, is a characteristic value of the fracture toughness K_{Ic} for stainless steel at room temperature [14]. The same source indicates that the K_{Ic} value will in fact increase as lower temperatures are considered, a fact that would further increase the stress relief in the crack tip region resulting from a martensitic phase transformation since more martensite would be present at higher values of K_I at the temperatures shown in Figs. 6a and 6b. The mode I opening stresses in Fig. 6 are a result of the total influence of martensitic phase transformation, i.e. the combined effects of both the volume expansion of the martensitic

phase and the increased yield stress of the transforming material. The former results in a lowering of the opening stress while the latter increases the stress level. The mode I opening stresses in Fig. 6 can thus be viewed as the net effect of these two mechanisms.

Having studied the temperature dependent appearance of the crack tip zones and how phase transformation influences the material behavior numerically through FE simulations, it is also of interest to determine these zones by an analytical approach. This is done in the next section by considering the elastic K_I field.

4 Plastic and transformed zones at the crack tip from the elastic K_I field

If mode I deformation is considered under plane strain conditions, the stress field in the vicinity of the crack tip can be obtained analytically from the elastic K_I-field. Using this stress field together with the transformation surface $h(\boldsymbol{\sigma}, z=0)=0$ in eq. (6), the shape of the transformed zone surrounding the crack tip can be calculated, cf. [18, 20]. In addition, the plastic zones may be obtained by assuming a von Mises yield condition. In this approach, the crack tip stress components are given by

$$\sigma_{ij} = \frac{K_I}{\sqrt{2\pi r}} \breve{\sigma}_{ij}(\theta) \tag{13}$$

where the functions $\breve{\sigma}_{ij}$ are given by

$$\begin{aligned} \breve{\sigma}_{xx} &= \cos\left(\frac{\theta}{2}\right)\left[1-\sin\left(\frac{\theta}{2}\right)\sin\left(\frac{3\theta}{2}\right)\right] \\ \breve{\sigma}_{yy} &= \cos\left(\frac{\theta}{2}\right)\left[1+\sin\left(\frac{\theta}{2}\right)\sin\left(\frac{3\theta}{2}\right)\right] \\ \breve{\sigma}_{xy} &= \cos\left(\frac{\theta}{2}\right)\sin\left(\frac{\theta}{2}\right)\cos\left(\frac{3\theta}{2}\right) \end{aligned} \tag{14}$$

Here θ and r are the polar crack tip coordinates, shown in Fig. 3. In addition, it is noted that $\sigma_{zz} = \nu(\sigma_{xx}+\sigma_{yy})$ for plane strain. First, assuming von Mises plasticity, the yield condition is defined by

$$\sqrt{3J_2} - \sigma_{\mathrm{y0}} = 0 \tag{15}$$

where σ_{y0} is the initial yield stress of the austenite phase as defined previously in eq. (4).

Using the stress components in eqs. (13)-(14), the radius of the plastic zone is obtained as

$$r_{\mathrm{pl}} = \frac{3}{2\pi}\left(\frac{K_I}{\sigma_{\mathrm{y0}}}\right)^2 \cos^2\left(\frac{\theta}{2}\right)\left[\sin^2\left(\frac{\theta}{2}\right)+\frac{1}{3}(1-2\nu)^2\right] \tag{16}$$

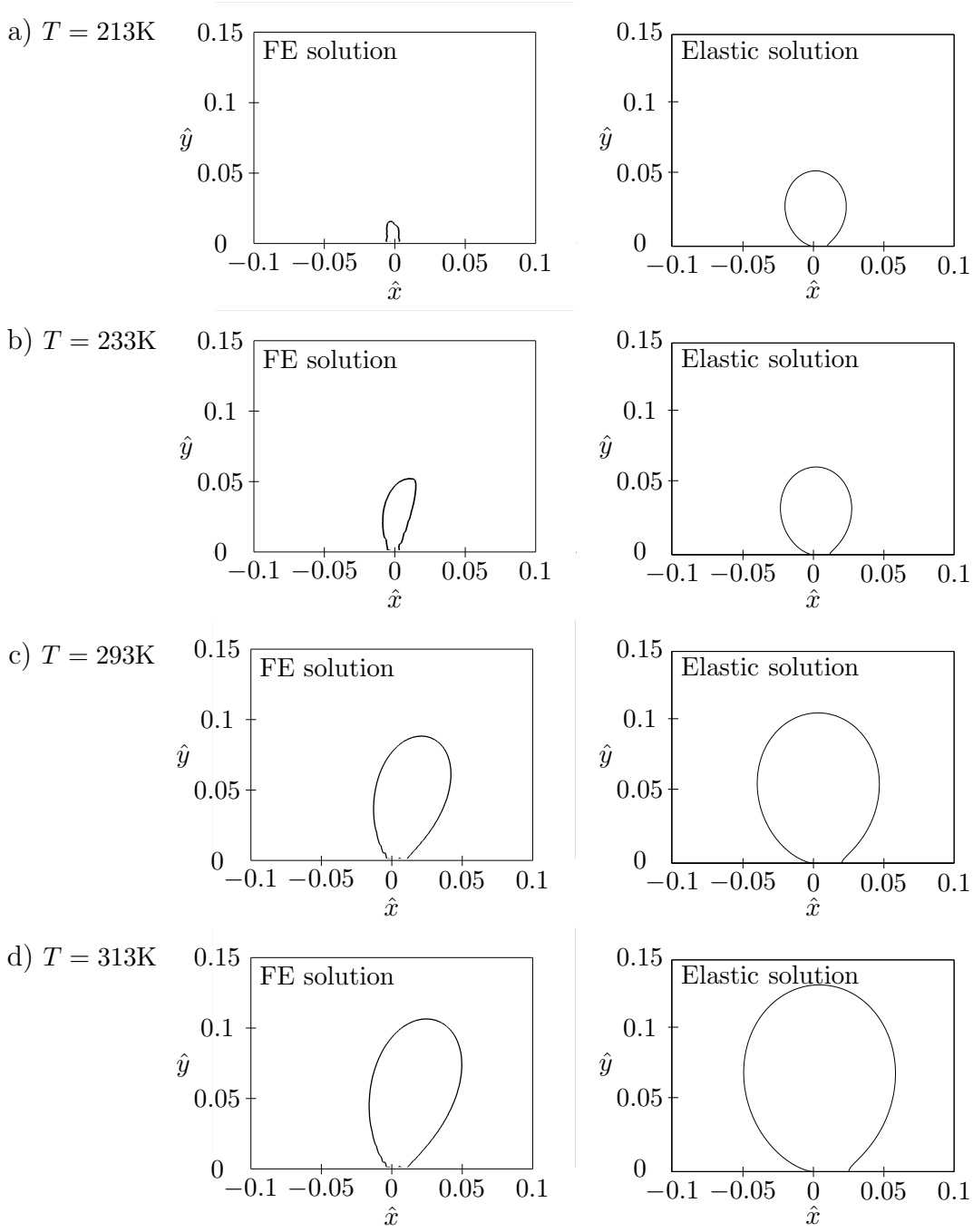

Figure 7: Size and shape of the plastic zones near the crack tip at four different temperatures under plane strain mode I conditions with $\nu = 0.3$ and $K_I = 33$ MPa$\sqrt{\text{m}}$. The left column shows FE results and the right column shows analytical results from the linear elastic stress field in eq. (16). The rows show results at each of the four different temperatures: (a) $T = 213$ K, (b) $T = 233$ K, (c) $T = 293$ K and (d) $T = 313$ K.

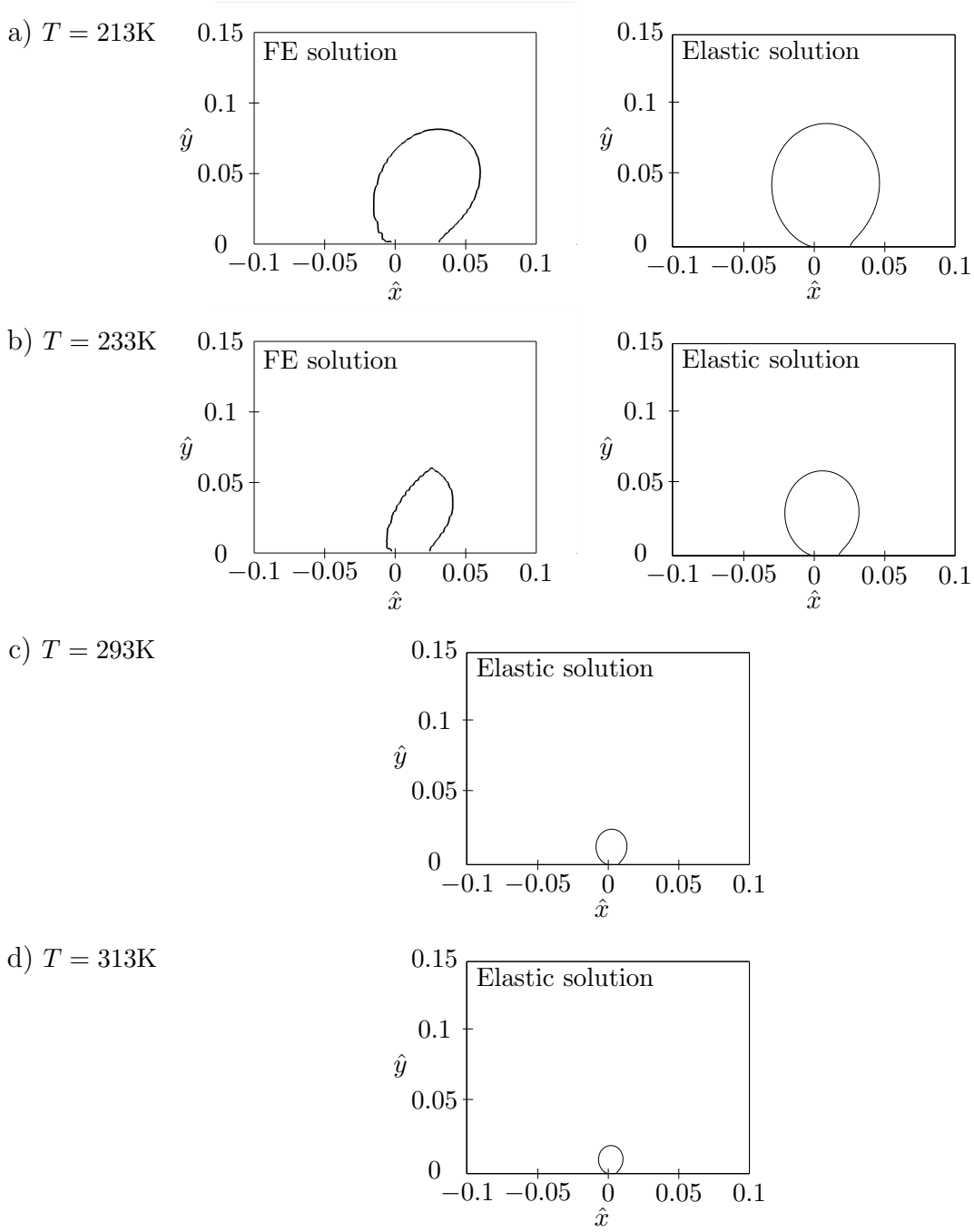

Figure 8: Size and shape of the transformed zones near the crack tip at four different temperatures under plane strain mode I conditions with $\nu = 0.3$, $K_I = 33$ MPa$\sqrt{\text{m}}$ and $z = 0$ from eq. (17). (a) $T = 213$ K, (b) $T = 233$ K, (c) $T = 293$ K and (d) $T = 313$ K. In figures (a) and (b), the left column shows FE results and the right column shows analytical results from the elastic solution. Note that no phase transformation is present in the FE results at the two higher temperatures of $T = 293$ K and $T = 313$ K in figures (c) and (d).

in the case of plane strain. On the other hand, the radius of the zone where phase transformation occurs is obtained by using the stress components in eqs. (13)-(14) together with the expression for the transformation surface in eq. (6). The radius of the transformation zone is then found as

$$r_{\mathrm{tr}} = \frac{1}{2\pi}\left(\frac{K_I \breve{F}_{\mathrm{mech}}\left(\theta\right)}{F_{\mathrm{trans}}\left(z,T\right) - F_{\mathrm{chem}}\left(T\right)}\right)^2 \tag{17}$$

Note that the notation $\breve{F}_{\mathrm{mech}}\left(\theta\right)$ indicates that this quantity is evaluated using only the $\breve{\sigma}_{ij}$-components of eq. (13), giving consistent units within the brackets of eq. (17).

The plastic zones obtained analytically from eq. (16) are plotted in Fig. 7 at four different temperatures under plane strain conditions with $\nu = 0.3$. The analytical transformation zones in Fig. 8 are calculated from eq. (17). In Figs. 7 and 8, $K_I = 33$ MPa$\sqrt{\mathrm{m}}$ is used as in the previous FE calculations. Note that the FE zones for $K_I = 33$ MPa$\sqrt{\mathrm{m}}$, cf. Figs. 4 and 5, are repeated in Figs. 7 and 8 for clarity. The solution obtained by employing the elastic K_I field is questionable when the transformation zone is confined within the plastic zone where the elastic field loses its applicability. This is due to inelastic deformation of the material, caused by phase transformation. However, the results in Figs. 7 and 8 show the same trends as found in the FE solution in Section 3. That is to say, at the lowest temperature of $T = 213$ K, the plastic zone is confined within the transformation zone and this gradually changes as the temperature is increased. At the higher temperatures of $T = 293$ K and $T = 313$ K, the plastic zones are larger than the transformed zones. Note that, due to the use of the elastic solution, the maximum extent of the zones is found at $\theta = 90^\circ$ unlike in the FE results where the zones are tilting into the first quadrant with $\theta \approx 70^\circ$. As the appearance of the transformation zones may not be valid since when they are well within the plastic zones, an alternative approach is called for where the plastic zones are treated explicitly. This can be achieved by considering the plastic solution obtained from the Hutchinson-Rice-Rosengren (HRR) field. This is elaborated in the next section.

5 Plastic and transformed zones at the crack tip from the HRR field

As an alternative approach to the elastic solution studied previously, the crack tip conditions can instead be analyzed using the stress field obtained from the HRR solution. Following [25, 26, 30], the inelastic behavior of the material is assumed to be described by a Ramberg-Osgood type of power hardening law, cf. [31], according to

$$\varepsilon = \frac{\sigma}{E}\left[1 + \alpha\left(\frac{\sigma}{\sigma_{\mathrm{y0}}}\right)^{n-1}\right] \tag{18}$$

where σ and ε are the uniaxial stress and strain, respectively, E is the elastic modulus, n is the strain hardening exponent, α is a material parameter and σ_{y0} is the initial yield stress of the austenite phase, as defined in eq. (4). Following [25], a generalized stress-strain relation is obtained from from eq. (18) according to

$$\varepsilon_{ij} = \frac{1}{E}\left[(1+\nu)\, s_{ij} + \frac{1-2\nu}{3}\sigma_{kk}\delta_{ij} + \frac{3}{2}\alpha\left(\frac{\sigma_{\text{eff}}}{\sigma_{y0}}\right)^{n-1} s_{ij}\right] \tag{19}$$

where $s_{ij} = \sigma_{ij} - \frac{1}{3}\sigma_{kk}\delta_{ij}$ is the deviatoric stress tensor and σ_{eff} the effective stress. Young's modulus E and the initial yield stress σ_{y0} were included in eq. (19) for consistency.

Letting r and θ denote the polar crack tip coordinates, as shown in Fig. 3, the crack tip stress components are, according to [25], given by

$$\sigma_{ij} = K_\sigma r^{-\frac{1}{n+1}} \widetilde{\sigma}_{ij}\left(\theta, n\right) \tag{20}$$

where K_σ is a stress amplitude parameter. The result in eq. (20) is arrived at by assuming the elastic energy to be much smaller than the plastic energy in the vicinity of the crack tip. Note that for $n = 1$, eq. (20) predicts a $1/\sqrt{r}$ singularity, consistent with linear elastic fracture mechanics theory, while larger values of the Ramberg-Osgood exponent will weaken the strength of the crack tip stress singularity.

Defining $s = (2n+1)/(n+1)$ according to [25], the angular dependence $\widetilde{\sigma}_{ij}\left(\theta, n\right)$ of the crack tip stress components is given by

$$\begin{aligned} \widetilde{\sigma}_{rr} &= s\phi + \frac{\partial^2\phi}{\partial\theta^2} \\ \widetilde{\sigma}_{\theta\theta} &= s\left(s-1\right)\phi \\ \widetilde{\sigma}_{r\theta} &= \left(1-s\right)\frac{\partial\phi}{\partial\theta} \end{aligned} \tag{21}$$

where $\phi = \phi\left(\theta, n\right)$ is obtained by solving a fourth-order differential equation for plane strain conditions as shown in [25]. The fourth-order differential equation is given as

$$\begin{aligned} \left[\frac{\partial^2}{\partial\theta^2} - n\left(s-2\right)\left\{n\left(s-2\right)+2\right\}\right]\left[\left(\widetilde{\sigma}_{\text{eff}}\right)^{n-1}\left\{s\left(2-s\right)\phi + \frac{\partial^2\phi}{\partial\theta^2}\right\}\right] \quad + \\ 4\left(s-1\right)\left\{n\left(s-2\right)+1\right\}\frac{\partial}{\partial\theta}\left[\left(\widetilde{\sigma}_{\text{eff}}\right)^{n-1}\frac{\partial\phi}{\partial\theta}\right] \quad = \quad 0 \end{aligned} \tag{22}$$

Note that ϕ is a function of the polar angle θ only, although different behavior for ϕ will be obtained for different values of the constant hardening exponent n. In [25], incompressibility is assumed which results in $\sigma_{zz} = \frac{1}{2}\left(\sigma_{rr} - \sigma_{\theta\theta}\right)$. This leads to the θ-dependence of the effective stress being given by

$$\widetilde{\sigma}_{\text{eff}}\left(n, \theta\right) = \left[\frac{3}{4}\left(\widetilde{\sigma}_{rr} - \widetilde{\sigma}_{\theta\theta}\right)^2 + 3\widetilde{\sigma}_{r\theta}^2\right]^{1/2} \tag{23}$$

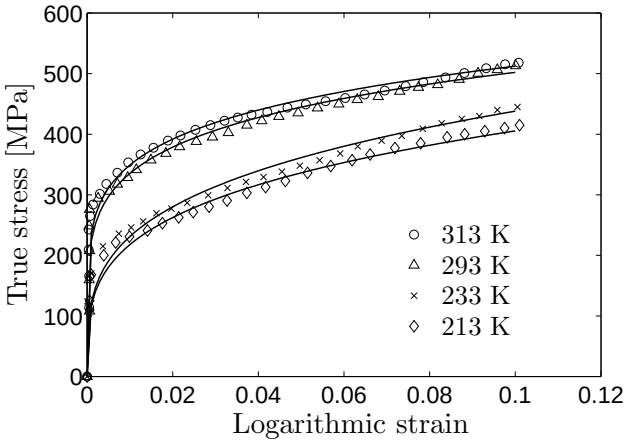

Figure 9: Ramberg-Osgood relation fit to experimental data taken from [27]. The corresponding Ramberg-Osgood parameter values are given in Table 3.

where it is noted that

$$\sigma_{\text{eff}} = K_\sigma r^{-\frac{1}{n+1}} \widetilde{\sigma}_{\text{eff}} \tag{24}$$

Finally, the angular dependence of the components in eqs. (21) must be normalized. Following [25, 30], this is done by defining

$$\hat{\sigma}_{ij} = \frac{\widetilde{\sigma}_{ij}}{\max\left(\widetilde{\sigma}_{\text{eff}}\right)} \tag{25}$$

In order to obtain the transformation zones for the material studied here, the parameters α and n must be determined. Considering the experimental data in [27] on SUS 304 austenitic stainless steel, as shown in Fig. 1, values of the parameters from the Ramberg-Osgood relation in eq. (18) were fit to experimental data, cf. Fig. 9.

Parameters found are summarized in Table 3. Note that the Ramberg-Osgood parameters are determined for an interval of relatively small strains, Fig. 1, namely less than 10 %. This value of strain was chosen so that the Ramberg-Osgood model could be properly fitted to the data. This also motivates the choice of $K_I = 33$ MPa$\sqrt{\text{m}}$ in the previous sections.

A comparison of the normalized stress components determined from the plane strain solution of the HRR field at the temperatures presently under consideration is shown in Fig. 10. Note that the angular dependence of the stress components is identical at $T = 293$ K and $T = 313$ K since $n = 2.6$ at both of these temperatures, cf. Fig. 10c and Table 3. Note that Fig. 10 shows the angular variation of the stress components for values of the n-parameter used in the present study, cf. Table 3, while the behavior for $n = 3$ and $n = 13$ is shown in [25].

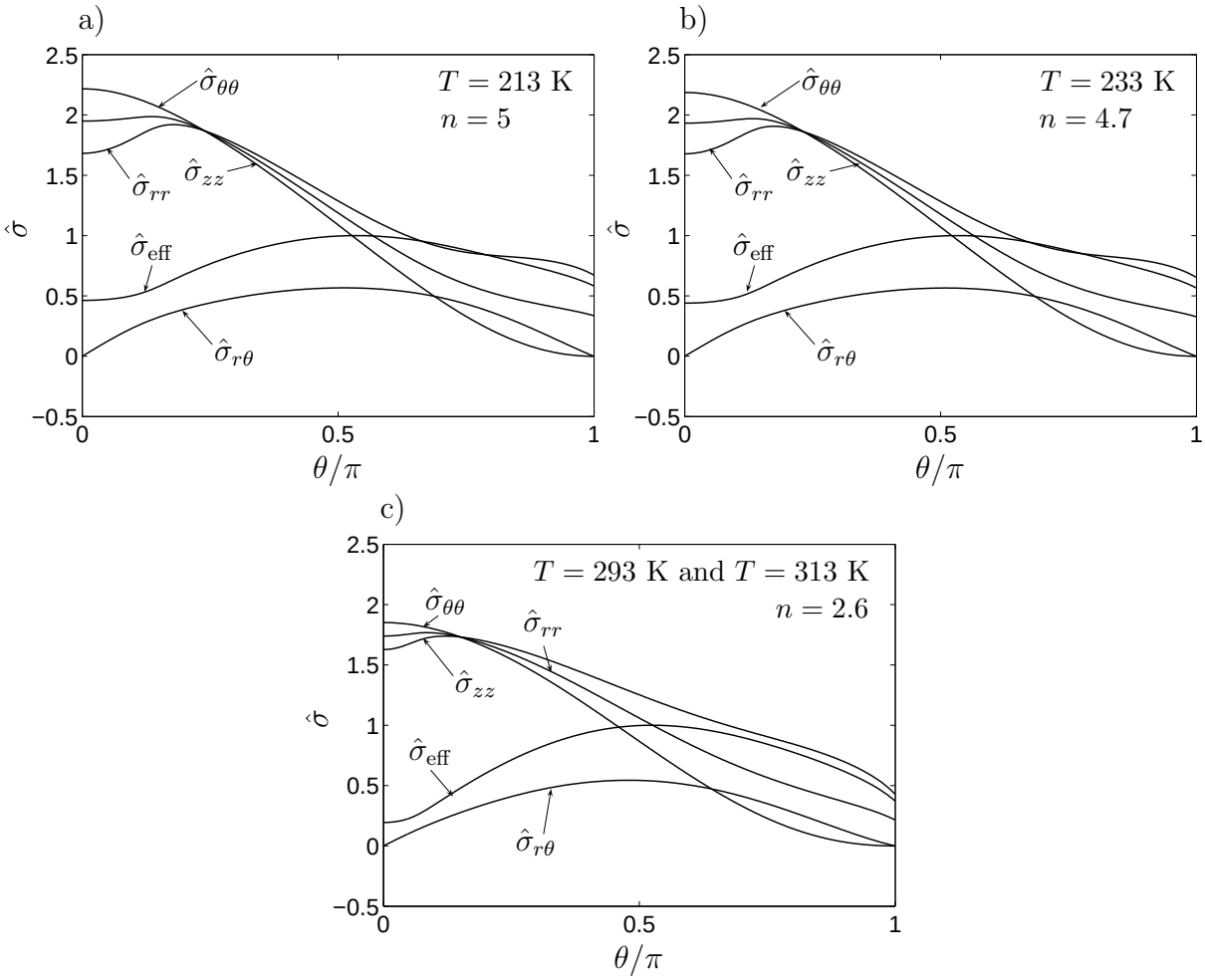

Figure 10: Angular dependence of the plane strain HRR crack tip stress components at the different temperatures studied in the present work. The stresses are normalized according to eq. (25). (a) $T = 213$ K, $n = 5$, $\alpha = 1.0$, (b) $T = 233$ K, $n = 4.7$, $\alpha = 1.4$, (c) $T = 293$ K, $n = 2.6$, $\alpha = 6.5$ and $T = 313$ K, $n = 2.6$, $\alpha = 7.5$.

Considering the von Mises yield condition in eq. (15) and using the effective stress in

Table 3: Parameters α and n in the Ramberg-Osgood relation calibrated against uniaxial data on SUS 304 stainless steel at four different temperatures, see Fig. 9.

T [K]	α	n
213	1.0	5.0
233	1.4	4.7
293	6.5	2.6
313	7.5	2.6

eq. (23), it is possible to obtain an estimate of the initial plastic zone radius according to

$$r_{\mathrm{pl}} = \left(\frac{K_\sigma \widetilde{\sigma}_{\mathrm{eff}} \left(\theta, n\right)}{\sigma_{\mathrm{y0}}} \right)^{n+1} \tag{26}$$

Next, by substituting eq. (20) into the expression for the transformation function in eq. (6), i.e. for $h = 0$, the radius of the transformation zone is given by

$$r_{\mathrm{tr}} = \left(\frac{K_\sigma \widetilde{F}_{\mathrm{mech}} \left(\theta, n\right)}{F_{\mathrm{trans}} \left(z, T\right) - F_{\mathrm{chem}} \left(T\right)} \right)^{n+1} \tag{27}$$

In eq. (27), $\widetilde{F}_{\mathrm{mech}}$ was introduced to denote F_{mech} evaluated using the $\widetilde{\sigma}_{ij}$ stress components in eq. (21). Thus, $\widetilde{F}_{\mathrm{mech}}$ is dependent only on the polar coordinate θ and the value of the Ramberg-Osgood parameters n and α which are constant for a given temperature.

The plastic zones obtained from eq. (26) are plotted in Fig. 11 and the transformation zones obtained from eq. (27) are plotted in Fig. 12 at four different temperatures for $h\left(\boldsymbol{\sigma}, z = 0\right) = 0$. Since no K_I parameter is present in the HRR solution, the stress amplitude K_σ has to be chosen in some way to allow comparison between the HRR results and the results obtained from the linear elastic solution and from FEs. This means that K_σ has to be chosen in such a way that the maximum zone radius at a certain temperature is the same in the HRR solution as in the result from either FEs or from the linear elastic solution. In the present study K_σ is chosen as $K_\sigma = 298$ MPa$\cdot$m$^{1/(n+1)}$ which makes the heights of the plastic zones obtained from the HRR solution and from the linear elastic solution at $T = 313$ K match. The lower temperature of $T = 213$ K should be avoided since the plastic zone is well within the transformed region which could be ambiguous using the plastic HRR solution which does not consider phase transformation. At $T = 233$ K the transformed zone and the plastic zone are of comparable size, making also this choice ambiguous. The highest temperature of $T = 313$ K is chosen since martensitic phase transformation is negligible at this temperature. Choosing K_σ in this way will give matching maximum zone radii at one temperature while deviations will appear at the other temperatures. Despite these deviations, the trend in the changes of both the plastic and the transformation zone sizes with changing temperature matches those found in the linear elastic solutions and in the FE solutions. Again the Cartesian crack tip coordinates are normalized according to eqs. (12) with $K_I = 33$ MPa$\sqrt{\mathrm{m}}$.

By the present choice of K_σ, the maximum plastic zone radius in Fig. 11d, obtained from the HRR solution for the temperature of 313 K, is the same as for that of the plastic zone shown in Fig. 7d. The latter is obtained from the elastic solution at the same temperature. Note that Figs. 11 and 12 repeat the FE zones at $K_I = 33$ MPa$\sqrt{\mathrm{m}}$, cf. Figs. 4 and 5, for convenience. As was noted in Section 3, the zone shapes remain similar for each isothermal case, irrespective of the load level. Considering the plastic zones obtained from

the HRR solution in Fig. 11, it can be noted that the height of the zones is fairly well approximated by the HRR solution compared to the FE zones at $T = 213$ K and at the higher temperature of $T = 293$ K. Note that at $T = 213$ K the plastic zone is well within the transformed region and the result from the HRR solution in Fig. 11a should be viewed with some caution. In passing it is also noted that the transformation stresses could be obtained from the transformation function h in eq. (6), much in the same way as was done for the stresses in the plastic HRR solution. At $T = 233$ K, Fig. 11b, where the plastic and martensitic zones are of comparable size, the HRR solution underestimates the size of the plastic zone compared to FEs. When it comes to the transformed zones shown in Fig. 12, it can be noted that the transformed zone obtained from the HRR solution at $T = 213$ K is significantly larger than the corresponding FE zone. At $T = 233$ K the HRR solution underestimates the size of the transformed zone, as is the case also with the plastic zone at the same temperature shown in Fig. 11b. At the higher temperatures of $T = 293$ K and $T = 313$ K, small transformed zones are obtained using the HRR solution, Figs. 12c and d, whereas no transformation zones are distinguishable using FEs at these temperatures.

As in Section 3, the competition between plastic and transformational strains is noticeable in the FE results in Figs. 11b and 12b where the plastic and phase transformation zones are of comparable size. This results in the pointed appearance of the FE zones at $T = 233$ K. The corresponding zones from the HRR solution are, however, smooth since they are based on an entirely plastic solution, not influenced by phase transformation.

By comparing Figs. 8 and 12, it can be noted that the size of the transformation zones is drastically reduced at the higher temperatures of $T = 293$ K and $T = 313$ K when using the HRR field. This may be attributed to the fact mentioned previously, that the elastic field will not give the correct transformation zone when it is confined within the plastic region. It can also be noted by comparing Figs. 7 and 11 that both the elastic solution and the HRR solution result in the maximum plastic zone radii appearing at an angle of $\theta \approx 90°$. Note that the plastic zones from the HRR solution are inclined by slightly more than 90°. It is emphasized that the analytical zones in Figs. 12a and b are obtained using the plastic HRR solution in spite of the fact that the plastic zones are within the transformed region. If eq. (16) is considered, the maximum radius of the plastic zone can be calculated by setting $\nu = 1/3$ and $\theta = \pi/2$, giving $r_{\mathrm{pl,max}} = 0.128\,(K_I/\sigma_{\mathrm{y0}})^2$. In [32], the maximum radius of the plastic zone is calculated using FEs, resulting in $r_{\mathrm{pl,max}} = 0.157\,(K_I/\sigma_{\mathrm{y0}})^2$ at $\theta = 70°$. Similar results are obtained in [33] where $r_{\mathrm{pl,max}} = 0.152\,(K_I/\sigma_{\mathrm{y0}})^2$ for $\theta = 71°$. In both cases plane strain conditions and elastic perfectly plastic material behavior are assumed. The plastic zones are in these publications found to be inclined at an approximate angle of 70° from the horizontal plane, which is also found in the present work when using FEs, cf. Fig. 11. The same behavior is also discussed in the review paper [34].

6 Concluding remarks

By employing a constitutive model for finite strain plasticity influenced by martensitic phase transformation under isothermal conditions, the material behavior in the vicinity of a mode I crack is studied in detail. The shape and size of the plastic zone is by this approach possible to compare to that of the zone where the austenitic microstructure is to some extent transformed into martensite. In accordance with several studies, found in the literature, the maximum extent of the plastic zones is found to be inclined approximately 70° from the horizontal axes in the FE results rather than the 90° found in the linear elastic solutions and the angle slightly larger than 90° found in the non-linear elasto-plastic HRR solutions. As observed in experiments, the temperature dependence of the martensitic phase transformation manifests itself by extensive phase transformation occurring at sub-zero temperatures while little or no phase transformation is to be found at room temperature and above. Also in accordance with experimental evidence found in the literature, the transformation zones appear with a butterfly shape close to the crack tip.

The influential presence of hard martensite results in transformation toughening of the crack tip region at lower temperatures, leading to a lowered mode I opening stress ahead of the crack tip. This is in contrast to the behavior at higher temperatures where the more ductile austenite is more or less unaffected by phase transformation. These aspects are herein illustrated by plotting the opening stress in front of the crack tip at different temperatures.

If the constitutive model is used together with an analytical linear elastic solution, the plastic zone and the zone where phase transformation has taken place deviate from the numerical FE results. Although the size and shape of the plastic and the transformed zones deviate, it is noted that the trends in the changes of the zone sizes with temperature is correct. In addition, from the linear elastic analytical solution the plastic zone is found to be confined within the phase transformation-exposed material at lower temperatures, whereas at higher temperatures, the plastic zone is much larger than the region where martensite formation has occurred. At $T = 233$ K the plastic zone and the transformation zone are of comparable size. Since the analytical elastic solution, at higher temperatures, results in the plastic zone enclosing any material containing martensite, the appearance of the phase transformation zone is ambiguous.

As an alternative approach, an HRR solution is obtained analytically, not least revealing that the linear elastic solution overestimates the phase transformation zone at higher temperatures. These analytical results agree with the FE solution. The plastic zones from the HRR solution are generally smaller than those obtained from the linear elastic solutions. It should be noted, however, that the HRR zones are obtained for a certain choice of the stress amplitude parameter K_σ at $T = 313$ K to allow comparison between results from the HRR solution with those from the linear elastic solution and from FEs. At higher

temperatures, where little or no martensite formation takes place, the linear elastic solution tends to overestimate the size of the transformed zones whereas the HRR solution agrees quite well with the FE solution at these temperatures. The HRR solution also renders plastic zones that have their maximum extent inclined slightly more than 90° from the horizontal axes. This is in contrast to the 70° inclination of the zones discussed previously in the literature, also obtained through FE simulations in the present work.

Through the present study, where FE simulations are studied in conjunction with both linear elastic and non-linear elasto-plastic analytical solutions, a thorough study of the material behavior near the tip of a mode I crack in austenitic stainless steel at different temperatures is performed. Novel insight into crack tip plasticity in this material when exposed to phase transformation, as well as into related transformation toughening, is given in the present work. As continued work, it would be interesting to consider quasi-static propagation of the crack to examine other aspects of transformation toughening.

References

[1] S.D. Antolovich and D. Fahr. An experimental investigation of the fracture characteristics of TRIP alloys. *Eng Fract Mech*, 4:133–144, 1972.

[2] S.D. Antolovich and B. Singh. On the toughness increment associated with the austenite to martensite phase transformation in TRIP steels. *Metall Trans*, 2:2135–2141, 1971.

[3] G.R. Chanani, S.D. Antolovich, and W.W. Gerberich. Fatigue crack propagation in Trip steels. *Metall Trans*, 3:2661–2672, 1972.

[4] E.R. Parker and V.F. Zackay. Enhancement of fracture toughness in high strength steel by microstructural control. *Eng Fract Mech*, 5:147–165, 1973.

[5] G.B. Olson. Transformation plasticity and toughening. *J de Phys IV*, 6:407–418, 1996.

[6] C.Y. Huo and H.L. Gao. Strain-induced martensitic transformation in fatigue crack tip zone for a high strength steel. *Mater Charact*, 55:12–18, 2005.

[7] Y. Iwasaki and Y. Nakasone. Distributions of α' martensitic phase transformed on fracture surfaces of SUS 304 stainless steel having through- and part-through-thickness fatigue cracks. *Key Eng Mat*, 353-358:319–322, 2007.

[8] A. Das and S. Tarafder. Experimental investigation on martensitic transformation and fracture morphologies of austenitic stainless steel. *Int J Plast*, 25:2222–2247, 2009.

[9] S.D. Antolovich and G.R. Chanani. Subcritical crack growth of TRIP steels in air under static loads. *Eng Fract Mech*, 4:765–776, 1972.

[10] Z. Mei and J.W. Morris. Analysis of transformation-induced crack closure. *Eng Fract Mech*, 39:569–573, 1991.

[11] K.V. Sudhakar and E.S. Dwarakadasa. A study on fatigue crack growth in dual phase martensitic steel in air environment. *Bull Mater Sci*, 23:193–199, 2000.

[12] S. Socrate. *Mechanics of microvoid nucleation and growth in high-strength metastable austenitic steels*. PhD thesis, Department of Mechanical Engineering, Massachusets Institute of Technology, 1995.

[13] R.G. Stringfellow. *Mechanics of strain-induced transformation toughening in metastable austenitic steels*. PhD thesis, Department of Mechanical Engineering, Massachusets Institute of Technology, 1990.

[14] Y. Oshida and A. Deguchi. Martensite formation and the related toughness in 304 stainless steel during low temperature fatigue. *Fatigue Fract Eng M*, 10:363–372, 1987.

[15] A. Bag, K.K. Ray, and E.S. Dwarakadasa. Influence of martensite content and morphology on the toughness and fatigue behavior of high-martensite dual-phase steels. *Metall Mater Trans A*, 32:2207–2217, 2001.

[16] S. Chatterjee and H.K.D.H. Bhadeshia. TRIP-assisted steels: cracking of high-carbon martensite. *Mater Sci Tech*, 22:645–649, 2006.

[17] S.-M. Kang and H. Kwon. Fracture behavior of intercritically treated complex structure in medium-Carbon 6Ni steel. *Metall Trans A*, 18:1587–1592, 1987.

[18] S. Yi and S. Gao. Fracture toughening mechanism of shape memory alloys due to martensite transformation. *Int J Solids Struct*, 37:5315–5327, 2000.

[19] G.Z. Wang. Effects of notch geometry on stress-strain distribution, martensite transformation and fracture behavior in shape memory alloy NiTi. *Mater Sci Eng A*, 434:269–279, 2006.

[20] Y. Freed and L. Banks-Sills. Crack growth resistance of shape memory alloys by means of a cohesive zone model. *J Mech Phys Solids*, 55:2157–2180, 2007.

[21] T. Iwamoto and T. Tsuta. Computational simulation on deformation behavior of CT specimens of TRIP steel under mode I loading for evaluation of fracture toughness. *Int J Plasticity*, 18:1583–1606, 2002.

[22] H. Hallberg and M. Ristinmaa. Modeling of crack behavior in austenitic stainless steel influenced by martensitic phase transformation. *Key Eng Mat*, 452-453:637–640, 2011.

[23] H. Hallberg, P. Håkansson, and M. Ristinmaa. A constitutive model for the formation of martensite in austenitic steels under large strain plasticity. *Int J Plasticity*, 23:1213–1239, 2007.

[24] H. Hallberg, P. Håkansson, and M. Ristinmaa. Thermo-mechanically coupled model of diffusionless phase transformation in austenitic steel. *Int J Solids Struct*, 47:1580–1591, 2010.

[25] J.W. Hutchinson. Singular behaviour at the end of a tensile crack in a hardening material. *J Mech Phys Solids*, 16:13–31, 1968.

[26] J.R. Rice and G.F. Rosengren. Plane strain deformation near a crack tip in a power-law hardening material. *J Mech Phys Solids*, 16:1–12, 1968.

[27] M.O. Onyuna. *Deformation behaviour and martensitic transformations in metastable austenitic steels and low alloyed multiphase steels*. PhD thesis, Department of Materials Science and Technology, Freiberg University of Mining and Technology, 2003.

[28] G. B Olson and M. Cohen. A mechanism for the strain-induced nucleation of martensitic transformations. *J Less Common Metals*, 28:107–118, 1972.

[29] M. Berveiller and F. D. Fischer, editors. *Mechanics of Solids with Phase Changes*. Number 368 in CISM Courses and Lectures. Springer Wien New York, 1997.

[30] J.W. Hutchinson. Fundamentals of the phenomenological theory of nonlinear fracture mechanics. *J Appl Mech-T ASME*, 50:1042–1051, 1983.

[31] W. Ramberg and W.R. Osgood. Description of stress-strain curves by three parameters. Technical Report 902, National Advisory Committee For Aeronautics, Washington DC, 1943.

[32] N. Levy, P.V. Marcal, W.J. Ostergren, and J.R. Rice. Small scale yielding near a crack in plane strain: A finite element analysis. *Int J Fracture*, 7:143–156, 1971.

[33] J.R. Rice and D.M. Tracey. Computational fracture mechanics. In S.J. Fenves, N. Perrone, A.R. Robinson, and W.C. Schnobrich, editors, *Numerical and Computer Methods in Structural Mechanics*, pages 585–623. Academic Press Inc. Orlando, Florida, USA, 1973.

[34] J.R. Rice, R.M. McMeeking, D.M. Parks, and E.P. Sorensen. Recent finite element studies in plasticity and fracture mechanics. *Comput Method Appl M*, 17/18:411–442, 1979.

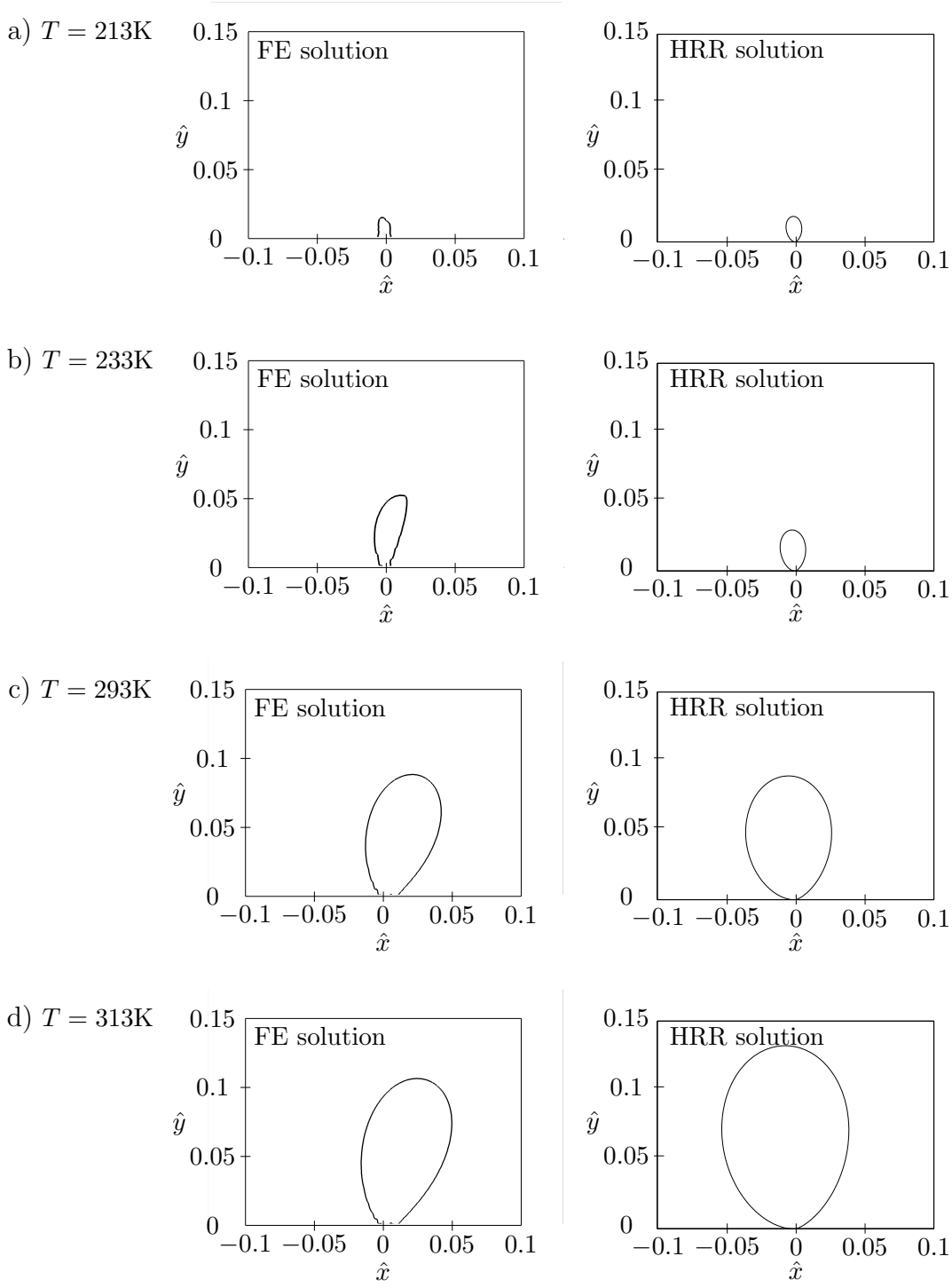

Figure 11: Size and shape of the plastic zones near the crack tip at four different temperatures under plane strain mode I conditions with $\nu = 0.3$. The left column shows FE results with $K_I = 33$ MPa$\sqrt{\text{m}}$ and the right column shows analytical results from the HRR solution with $K_\sigma = 298$ MPa·m$^{1/(n+1)}$. The rows show results at each of the four different temperatures: (a) $T = 213$ K, (b) $T = 233$ K, (c) $T = 293$ K and (d) $T = 313$ K.

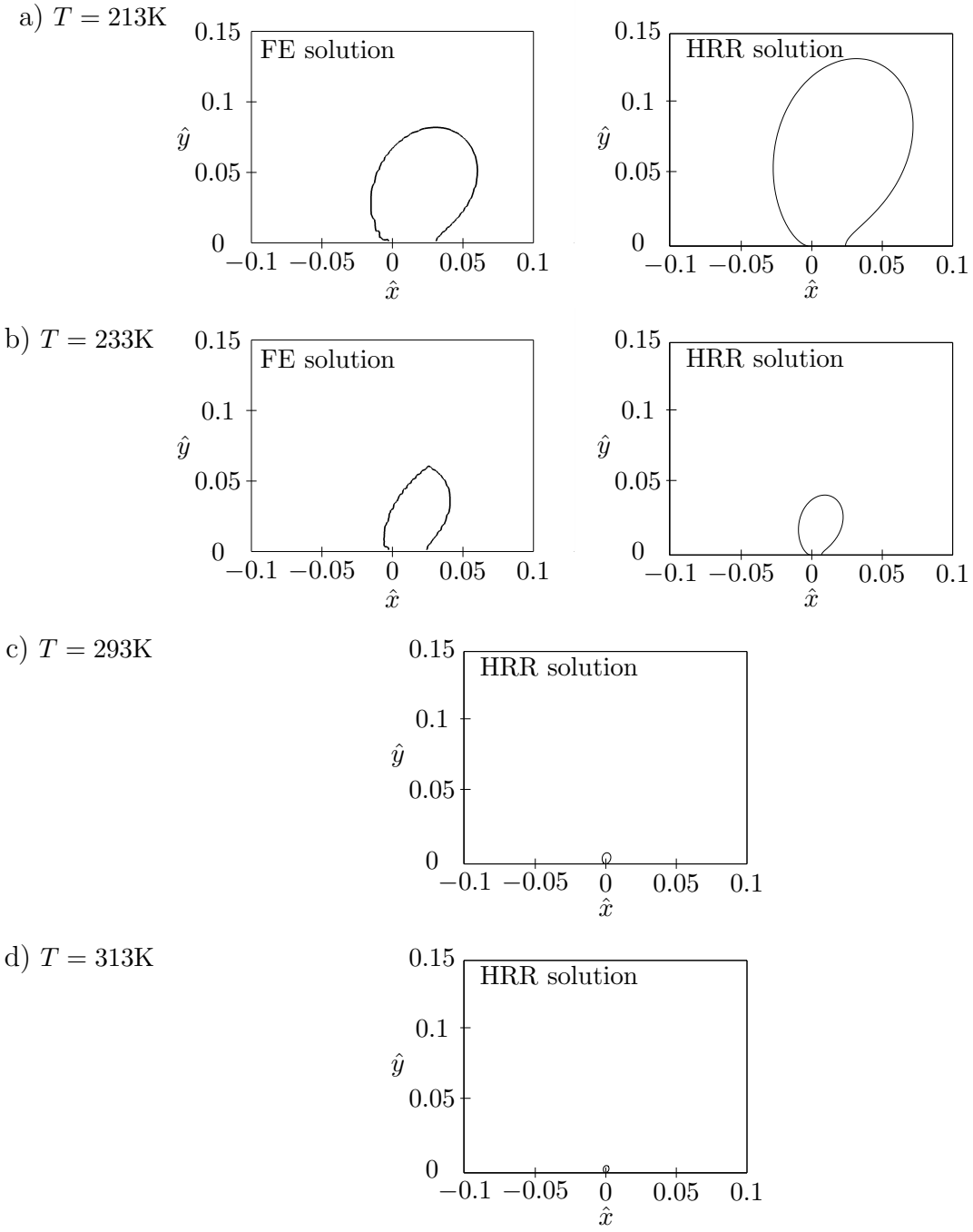

Figure 12: Size and shape of the transformed zones near the crack tip under plane strain mode I conditions with $\nu = 0.3$. (a) $T = 213$ K, (b) $T = 233$ K, (c) $T = 293$ K and (d) $T = 313$ K. In figures (a) and (b), the left column shows FE results with $K_I = 33$ MPa$\sqrt{\text{m}}$ and the right column shows results from the HRR solution with $K_\sigma = 298$ MPa·m$^{1/(n+1)}$. Note that no phase transformation occurs in the FE results at the two higher temperatures.